

# Self-Assembled Cu–Sn–S Nanotubes with High (De)Lithiation Performance

Jie Lin,<sup>†,‡,§,||</sup> Jin-Myoung Lim,<sup>§</sup> Duck Hyun Youn,<sup>‡,⊥</sup> Kenta Kawashima,<sup>‡,||</sup> Jun-Hyuk Kim,<sup>‡</sup> Yang Liu,<sup>‡,§,||</sup> Hang Guo,<sup>\*,†,||</sup> Graeme Henkelman,<sup>\*,§,||</sup> Adam Heller,<sup>‡</sup> and Charles Buddie Mullins<sup>\*,‡,||</sup>

<sup>†</sup>Pen-Tung Sah Micro-Nano Science and Technology Institute, Xiamen University, Xiamen, Fujian 361005, China

<sup>‡</sup>Department of Chemical Engineering and Department of Chemistry, Center for Electrochemistry, University of Texas at Austin, Austin, Texas 78712-0231, United States

<sup>§</sup>Department of Chemistry and the Institute for Computational Engineering and Sciences, University of Texas at Austin, Austin, Texas 78712-0165, United States

<sup>⊥</sup>Department of Chemical Engineering, Kangwon National University, Chuncheon, Gangwon-do 24341, South Korea

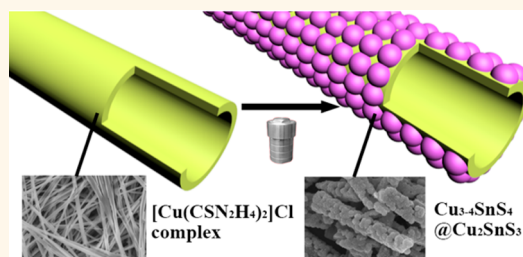
<sup>#</sup>College of Chemistry and Chemical Engineering, Central South University, Changsha, Hunan 410083, China

<sup>||</sup>Texas Materials Institute, University of Texas at Austin, Austin, Texas 78712-1591, United States

## Supporting Information

**ABSTRACT:** Through a gelation–solvothoermal method without heteroadditives, Cu–Sn–S composites self-assemble to form nanotubes, sub-nanotubes, and nanoparticles. The nanotubes with a  $\text{Cu}_{3-4}\text{SnS}_4$  core and  $\text{Cu}_2\text{SnS}_3$  shell can tolerate long cycles of expansion/contraction upon lithiation/delithiation, retaining a charge capacity of  $774 \text{ mAh g}^{-1}$  after 200 cycles with a high initial Coulombic efficiency of 82.5%. The importance of the Cu component for mitigation of the volume expansion and structural evolution upon lithiation is informed by density functional theory calculations. The self-generated template and calculated results can inspire the design of analogous Cu–M–S (M = metal) nanotubes for lithium batteries or other energy storage systems.

**KEYWORDS:** copper tin sulfide, nanotube, core–shell, gelation–solvothoermal, density functional theory, lithium battery



Tin-based sulfides are prospective electrodes for lithium-ion batteries (LIBs),<sup>1</sup> due to the high lithiation ability of Sn ( $\sim 4.4 \text{ Li}$  for per Sn)<sup>2</sup> and large interlayer spacings ( $c = 0.5899/0.4330$  for  $\text{SnS}/\text{SnS}_2$ )<sup>3,4</sup> for energy storage. However, the lithiation potentials of tin-based composites<sup>5</sup> are too low to be exploited as cathodes in Li metal batteries.<sup>6</sup> Introducing a metallic component with a high electrochemical potential can improve the specific energy.<sup>7</sup> Cu–Sn–S (CTS), a low-toxicity and earth-abundant ternary alloy, has a high specific capacity and superior energy density compared with other Cu/Sn-based sulfides in Li metal batteries (Table S1 and Figure S1). The large interlayer and tunnel sizes of CTS are also advantageous for Li diffusion,<sup>8</sup> so a few studies<sup>9–14</sup> (mostly  $\text{Cu}_2\text{SnS}_3$  particles) have explored its potential use in LIBs, but there has been a lack of detailed investigations regarding the phase composition and structural evolution upon lithiation. On the other hand, the highly lithiated products are accompanied by huge volume expansion leading to rapid capacity degradation. Nanostructured materials can help accommodate the adverse stress,<sup>15</sup> especially one-dimensional nanomaterials, including Cu@SnS nanowires,<sup>16</sup>  $\text{SnS}_2$ @ $\text{SiO}_2$  nanorods,<sup>17</sup> and Sn@carbon nanotubes.<sup>18</sup> But most of them are fabricated by using constrained templates

(e.g., anodic alumina<sup>16</sup> and carbon nanotube<sup>18,19</sup>) and heteroadditives (template agent, surfactant, catalyst, etc.).<sup>17,20</sup> Core–shell<sup>21</sup> or gradient structures<sup>22</sup> with changing stoichiometries in the  $\text{LiNi}_{1-x}\text{M}_x\text{O}_2$  (M = metal) cathodes can be effective for improving cyclability.<sup>23</sup> However, this idea has been rarely applied to Li-free electrodes (rather than core–shell heteromaterials) due to the difficulties in synthesis and characterization. Moreover, no work has been reported about one-dimensional CTS materials for LIBs.

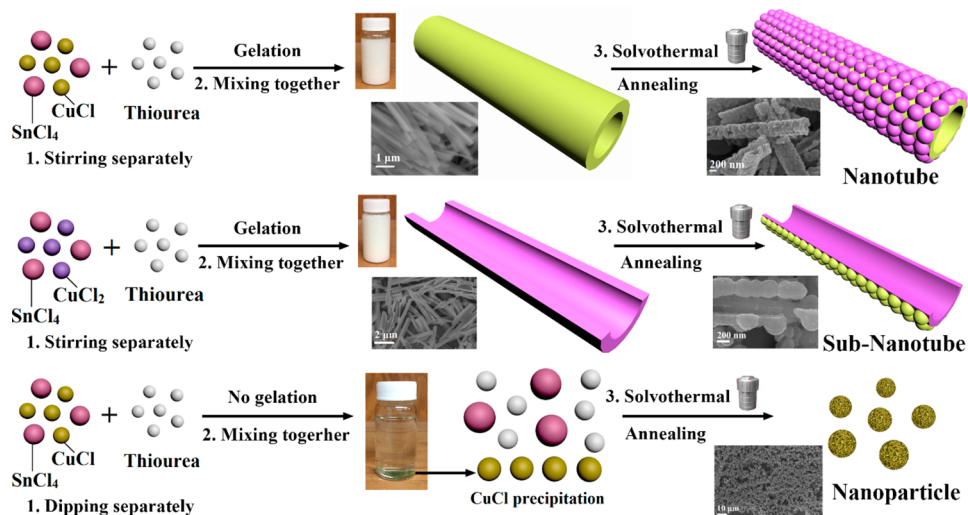
For the above reasons, we combine gelation and solvothoermal methods to synthesize the CTS nanotubes (NTs), sub-nanotubes (SNTs), and nanoparticles (NPs) without heteroadditives, as illustrated in Scheme 1, and the related processes are described in detail in the Methods. Material characterizations reveal the core–shell structure of  $\text{Cu}_{3-4}\text{SnS}_4$ @ $\text{Cu}_2\text{SnS}_3$  in the CTS NTs, facilitating the highest charge capacity of  $774 \text{ mAh g}^{-1}$  after 200 cycles. Additionally, we have constructed atomic scale models of the CTS materials with three different stoichiometries,

Received: July 26, 2017

Accepted: September 12, 2017

Published: September 12, 2017

Scheme 1. Synthetic processes of CTS NTs, SNTs, and NPs by Gelation–Solvothermal Methods.



based upon density functional theory (DFT) and global optimization using the basin-hopping algorithm. These DFT calculations provide insights into the volume expansion, electrochemical potentials, formation enthalpy, and structural changes of ternary alloy materials upon lithiation.

## RESULTS AND DISCUSSION

Utilizing the self-assembled CuCl–thiourea (Tu) complex nanotubes as shown in the scanning electron microscopy (SEM) images of Figure 1a,b, the homogeneous and porous CTS NTs (Figure 1c,d) are generated in the solvothermal process. The hollow nanotubes are composed of numerous CTS nanoparticles.

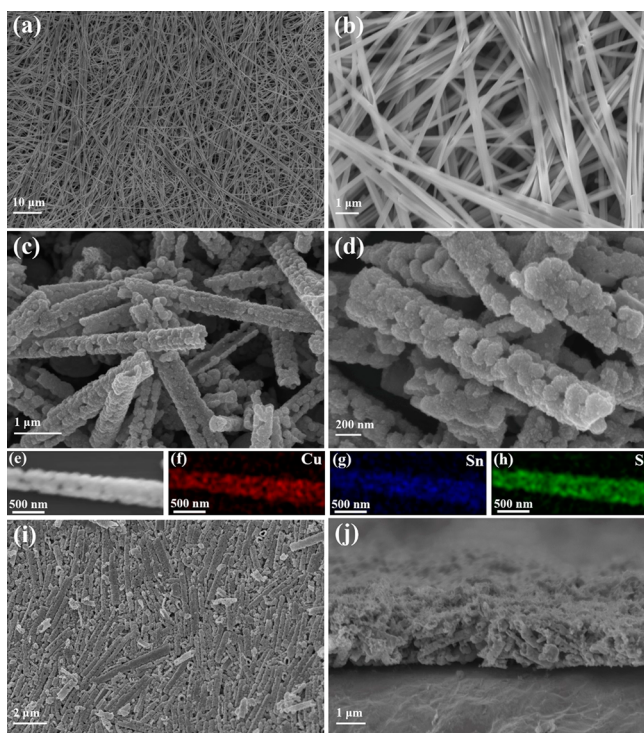


Figure 1. SEM images of (a, b) CuCl–Tu complex nanotubes, (c, d) CTS NTs, and (e–h) corresponding EDS elemental mappings. (i) Surface SEM image of stacked film and (j) cross-section SEM image of electrode film of CTS NTs.

The energy dispersive spectra (EDS) elemental mappings (Figure 1e–h) show that Cu, Sn, and S elements are uniformly distributed in the nanotubes. Owing to the flexible structure, the volume expansion can be accommodated for lithiation. In addition, the nanotubes are tightly packed (Figure 1i) and form a compact film as the electrode film (Figure 1j), reducing the consumption of  $\text{Li}^+$  for the formation of solid electrolyte interphase (SEI) film.

Derived of a  $\text{CuCl}_2$ –Tu complex to form imperfect sub-nanotubes (Figure 2a,b), Sn ions react with the precursor to assemble CTS SNTs (Figure 2c,d) in the solvothermal step. Unlike the CTS NTs, the EDS elemental mappings (Figure 2e–h) show that Cu, Sn, and S elements are distributed mainly on the surface and surrounding areas, signifying a different phase distribution and unstable divided structure for lithium storage. The crystal structures of the related complexes are shown in Figure S2. The surface areas and porosity of the CTS NTs and SNTs are also investigated by nitrogen absorption and desorption measurements (Figure S3), elucidating the larger specific surface area and pore size of the CTS SNTs compared to the CTS NTs.

The SEM images of the CTS NPs (Figure 2i,j) display that the CTS materials inside the dense particles are compact with a rough texture forming large aggregations. From the EDS elemental mappings (Figure 2k–n), Cu, Sn, and S elements tend to concentrate in the center, implying the sluggish  $\text{Li}^+$  penetration into the internal active materials and the triggered large volume expansion after full lithiation.

The X-ray diffraction (XRD) patterns of all samples (Figure 3a) show that the compounds representing the CTS NPs, SNTs, and NTs are indexed as  $\text{Cu}_2\text{SnS}_3$ ,  $\text{Cu}_3\text{SnS}_4$ , and  $\text{Cu}_4\text{SnS}_4$ , respectively. Figure 3b indicates that the CTS NPs are composed of only the  $\text{Cu}_2\text{SnS}_3$  phase. Figure 3c,d indicate that both the CTS SNTs and NTs contain a mix of the  $\text{Cu}_2\text{SnS}_3$ ,  $\text{Cu}_3\text{SnS}_4$ , and  $\text{Cu}_4\text{SnS}_4$  phases. The major compound for both the CTS SNTs and NTs is  $\text{Cu}_2\text{SnS}_3$ : 73.3% for the CTS SNTs and 48.6% for the CTS NTs. Figure 3c shows that the CTS SNTs consist of  $\text{Cu}_3\text{SnS}_4$  (23.0%) and  $\text{Cu}_4\text{SnS}_4$  (3.7%). In contrast, Figure 3d demonstrates that  $\text{Cu}_4\text{SnS}_4$  (37.2%) is a larger component of the CTS NTs than  $\text{Cu}_3\text{SnS}_4$  (14.2%). Therefore, it can be considered that the CTS SNTs more reflect the character of  $\text{Cu}_3\text{SnS}_4$ , while the CTS NTs reflect  $\text{Cu}_4\text{SnS}_4$ . The detailed relaxed atomic structures are

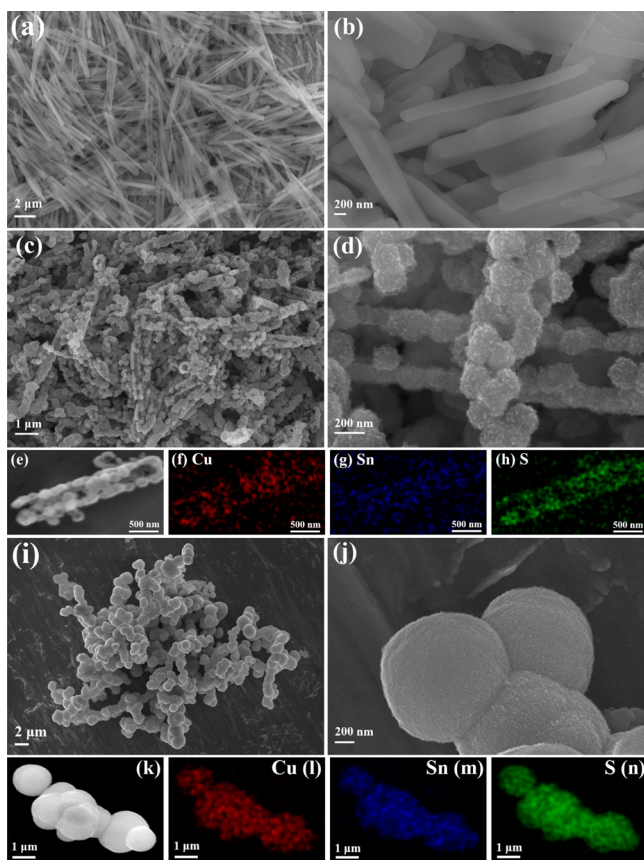


Figure 2. SEM images of (a, b)  $\text{CuCl}_2\text{-Tu}$  complex sub-nanotubes, (c, d) CTS SNTs, and (e–h) corresponding EDS elemental mappings. SEM images of (i, j) CTS NPs and (k–n) corresponding EDS elemental mappings.

displayed in Figure S4, and the calculated lattice parameters are listed in Table S2.

The transmission electron microscopy (TEM) images and corresponding selected area electron diffraction (SAED) patterns of the CTS NTs are shown in Figure 4a, displaying the hollow hierarchical structure with solid nanoparticles on the surface of the nanotubes. From the edge areas of the high-resolution TEM (HR-TEM) images (Figure 4b), two cross lattice fringes with interplanar spacings of 0.27 and 0.31 nm are indexed as the (200) and (111) crystal planes of  $\text{Cu}_2\text{SnS}_3$  (JCPDS 89-2877). All the diffraction spots of the outside (O) region (top-right inset of Figure 4a) are also indexed as the  $\text{Cu}_2\text{SnS}_3$  phase, while the diffraction spot array of the inside (I) region (bottom-left inset of Figure 4a) is indexed as the  $(\bar{1}02)$ , (122), and (220) facets along the  $[2\bar{2}1]$  orientation of  $\text{Cu}_4\text{SnS}_4$  (JCPDS 71-0129). The different core and shell phases are also confirmed by the scanning-TEM (STEM) mappings of the CTS NTs (Figure 4c–f), displaying some bright regions with more Cu and S; that is,  $\text{Cu}_{3-4}\text{SnS}_4$  phases exist inside the nanotubes.

The TEM images and related SAED patterns of the CTS SNTs are shown in Figure 4g, displaying the self-formed hollow nanoparticles on the surface of the imperfect sub-nanotubes. From the HR-TEM of the edge of the CTS SNTs (Figure 4h), the lattice fringes with an interplanar spacing of 0.29 nm are indexed as the (126) crystal plane of  $\text{Cu}_3\text{SnS}_4$  (JCPDS 36-0217) or the (112) crystal plane of  $\text{Cu}_4\text{SnS}_4$ . The diffraction spot array of the outside (O) region (top-right inset of Figure 4g) is indexed as the  $(\bar{2}12)$ , (434), and (622) facets along the  $[1\bar{8}5]$  direction of  $\text{Cu}_4\text{SnS}_4$ , while all the diffraction rings of the inside (I) region (bottom-left inset of Figure 4g) are indexed as the  $\text{Cu}_2\text{SnS}_3$  phase. The STEM mappings of the CTS SNTs (Figure 4i–l) confirm the porous nanotubes are composed of discrete nanoparticles, which are not tightly bound to each other, *i.e.*, a mechanically weak structure. The STEM elemental distributions

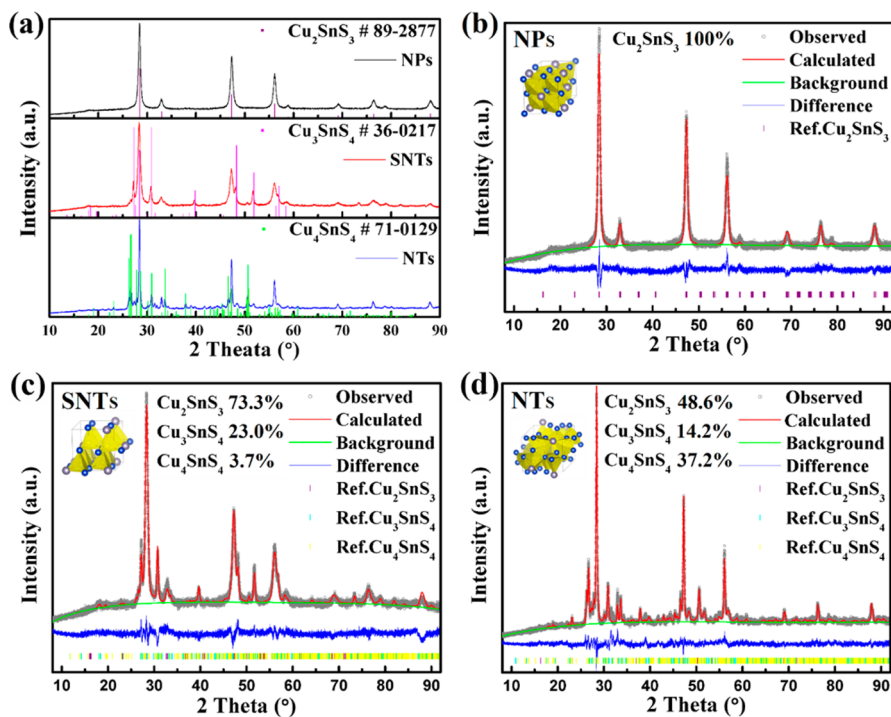
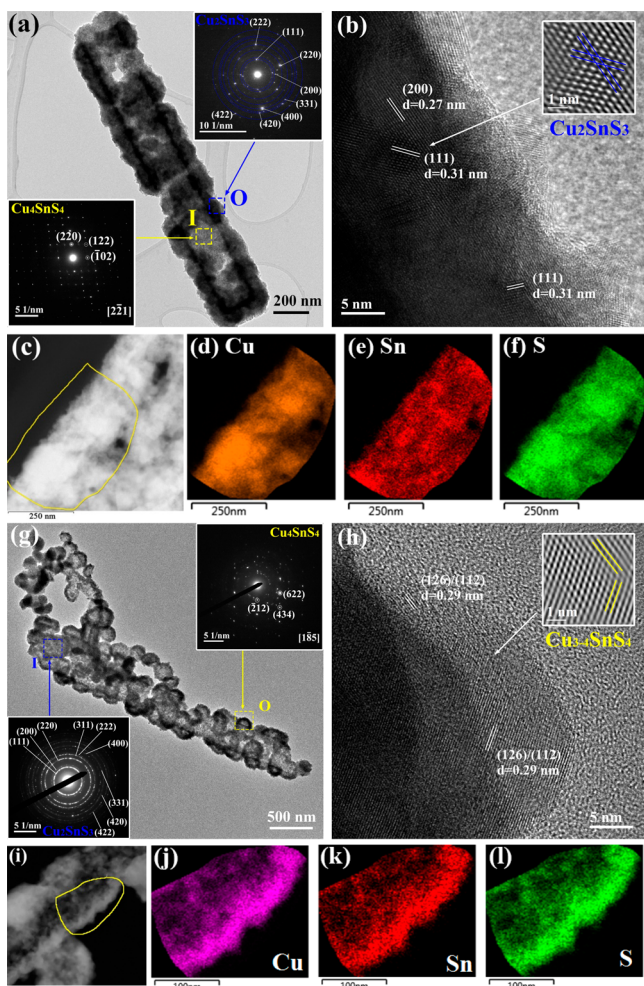


Figure 3. (a) XRD patterns and representative phases. (b–d) Rietveld refinements for XRD patterns of CTS NPs, SNTs, and NTs and representative atomic structures of  $\text{Cu}_2\text{SnS}_3$ ,  $\text{Cu}_3\text{SnS}_4$ , and  $\text{Cu}_4\text{SnS}_4$ . Atomic coloring: S, yellow; Cu, blue; Sn, gray.



**Figure 4.** (a) TEM images of CTS NTs and SAED patterns from outside and inside regions. (b) HR-TEM images of the surface on CTS NTs. (c–f) STEM elemental mappings of CTS NTs. (g) TEM images of CTS SNTs and SAED patterns from outside and inside regions. (h) HR-TEM images of the surface on CTS SNTs. (i–l) STEM elemental mappings of CTS SNTs.

of different regions and line scans in the CTS NTs and SNTs are specifically compared in Figure S5 and Table S3, verifying the core–shell elemental distributions of  $\text{Cu}_{3-4}\text{SnS}_4@ \text{Cu}_2\text{SnS}_3$  in the CTS NTs and  $\text{Cu}_2\text{SnS}_3@ \text{Cu}_{3-4}\text{SnS}_4$  in the CTS SNTs. The hollow hierarchical structure can also be seen from the cross-section SEM images of the nanotubes in the CTS NTs and SNTs (Figure S6), displaying smooth nanotubes inside and rough nanoparticles outside.

The X-ray photoelectron spectroscopy (XPS) peaks are similar in all samples (Figure S7), so the Auger spectra of Cu LMM (Figure 5a) is required to identify the valence states of Cu ions. In terms of chemical stoichiometry, Cu ions in  $\text{Cu}_2\text{SnS}_3$  and  $\text{Cu}_4\text{SnS}_4$  are likely to be  $\text{Cu}^+$ , but Cu ions of  $\text{Cu}_3\text{SnS}_4$  are both  $\text{Cu}^+$  and  $\text{Cu}^{2+}$ . As a result, the Cu LMM peak in the CTS SNTs slightly shifts to lower energy than in the CTS NPs and NTs, indicating the existence of  $\text{Cu}_3\text{SnS}_4$  with  $\text{Cu}^{2+}$  on the surface. To definitely understand the oxidation states of Cu ions in  $\text{Cu}_2\text{SnS}_3$ ,  $\text{Cu}_3\text{SnS}_4$ , and  $\text{Cu}_4\text{SnS}_4$ , we calculate the partial (projected) density of states (PDOS) using DFT calculations as shown in Figure 5b–d. Cu ions in  $\text{Cu}_2\text{SnS}_3$  (Figure 5b) and  $\text{Cu}_4\text{SnS}_4$  (Figure 5d) indicate fully and symmetrically filled 3d electrons (electron configuration of  $d^{10}$ ;  $\text{Cu}^+$ ) in Cu d orbitals.

In contrast, Figure 5c shows an oxidized 3d orbital of Cu ions in  $\text{Cu}_3\text{SnS}_4$ , indicating an incomplete  $d^{10}$  electron configuration ( $\text{Cu}^{1+-2+}$ ).

Based on the above results, the core–shell structures of the CTS SNTs and NTs are depicted in Figure 6a,b. The different structures influence the stability during (de)lithiation as illustrated in Figure 6c. The volume expansion of the  $\text{Cu}_2\text{SnS}_3$  core inside the CTS SNTs is larger than that of the  $\text{Cu}_{3-4}\text{SnS}_4$  core inside the CTS NTs, implying the nanoparticles on the surface are more likely to be peeled off after repeated (de)lithiation as simulated in Figure S8. The decomposition will lead to the collapse of nanotubes and the subsequent inferior cycling performance, which can be seen from the *post-mortem* morphology. After 200 cycles, the large aggregations composing the CTS NPs (Figure 6d) break into small particles. The weak structure of the CTS SNTs collapses into divided parts, and only a small fraction of the nanotubes can be found as marked in Figure 6e. In contrast, the original nanotube structure remains in the CTS NTs even after 200 cycles (Figure 6f), indicating the durability of the CTS NTs primarily composed of the  $\text{Cu}_4\text{SnS}_4$  phase.

To probe the materials characteristics with respect to volume expansion, we calculate the lithiated structures of  $\text{Cu}_2\text{SnS}_3$ ,  $\text{Cu}_3\text{SnS}_4$ , and  $\text{Cu}_4\text{SnS}_4$ . The DFT calculations are performed at different stages of lithiation and combined with the basin-hopping algorithm to find low-energy structures. In these calculations, we aim to insert 13 mol of Li after the formation of  $\text{Li}_2\text{S}$ ; thus, 19 mol of Li are inserted for  $\text{Cu}_2\text{SnS}_3$  and 21 mol of Li are inserted for both  $\text{Cu}_3\text{SnS}_4$  and  $\text{Cu}_4\text{SnS}_4$ . The resulting relative volume expansion is shown in Figure 6g as a function of lithiation stages, quantified by the Li/Sn ratio. As indicated in our previous report on SnS and  $\text{SnS}_2$  materials,<sup>1</sup> the volume expansion of the Sn–S anode is directly related to the S/Sn ratio so that  $\text{SnS}_2$  has a smaller volume expansion than SnS. Analogously, Figure 6g shows a larger volume expansion of  $\text{Cu}_2\text{SnS}_3$  than that of  $\text{Cu}_{3-4}\text{SnS}_4$ , because a larger fraction of S can form  $\text{Li}_2\text{S}$  upon lithiation and the  $\text{Li}_2\text{S}$  component acts as a volume buffer. Additionally,  $\text{Cu}_4\text{SnS}_4$  expands less than  $\text{Cu}_3\text{SnS}_4$ , implying that the Cu component has a synergistic role with Sn and S for reducing the volume expansion in the CTS materials. Figure 6h shows the calculated potentials for each component and the estimated capacity.  $\text{Cu}_2\text{SnS}_3$  has a lower potential and reaches a near-zero potential (Li/Sn = 10) earlier than the others.  $\text{Cu}_3\text{SnS}_4$  has a potential profile similar to  $\text{Cu}_4\text{SnS}_4$  but approaches 0 V (Li/Sn = 16) before  $\text{Cu}_4\text{SnS}_4$  (Li/Sn = 18). These calculations indicate that the larger volume expansion is correlated with lower potentials and smaller capacity. The potential profiles are derived from the convex hull plots, which are calculated from the formation enthalpy as a function of the normalized Li/Sn ratio (Figure 6i). The enthalpy of  $\text{Cu}_2\text{SnS}_3$  is located above instead of on the convex hull (normalized Li/Sn = 0.5–0.9), as well as those of  $\text{Cu}_3\text{SnS}_4$  (normalized Li/Sn = 0.15–0.4), implying these phases are likely to be unstable, and an inhomogeneous volume expansion will be caused by the phase separation. In contrast, the enthalpy points of  $\text{Cu}_4\text{SnS}_4$  are mostly on the convex curve, indicating a solid solution reaction with relatively stable intermediate phases.

Details of the structural evolution of the optimized configurations of  $\text{Cu}_2\text{SnS}_3$ ,  $\text{Cu}_3\text{SnS}_4$ , and  $\text{Cu}_4\text{SnS}_4$  are shown in Figure 6j–l. In the early lithiation stage, the structures are disordered with Cu bonding disrupting the  $\text{Li}_2\text{S}$  lattice. In the advanced lithiation stage, a stable  $\text{Li}_2\text{S}$  phase forms around an amorphous Li–Cu–Sn phase. Investigation of the structural

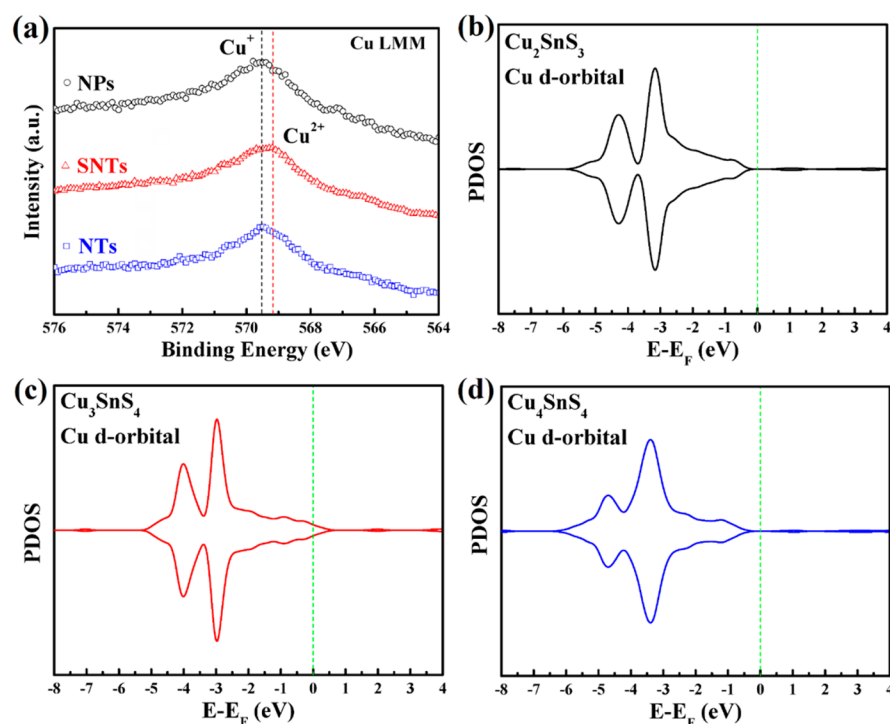
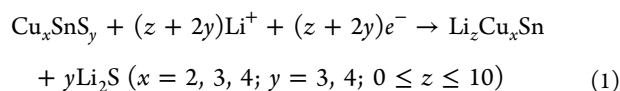


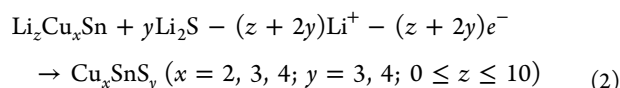
**Figure 5.** (a) Auger spectra of Cu LMM in CTS NPs, SNTs, and NTs. (b–d) PDOS of Cu d orbital in Cu<sub>2</sub>SnS<sub>3</sub>, Cu<sub>3</sub>SnS<sub>4</sub>, and Cu<sub>4</sub>SnS<sub>4</sub>. Green dotted line indicates Fermi level  $E = E_F$ .

evolution by *ex situ* XRD (Figure S9) shows that the diffraction peaks are similar in all samples. Choosing the XRD pattern of the CTS NPs (Figure 6m) as representative, the reduced (111) peak of samples after discharged to 1 V implies gradual decomposition of the Cu<sub>2</sub>SnS<sub>3</sub> phase. After discharged to 0.01 V, no peaks can be found except for those of the Cu substrate, consistent with the amorphous lithiated Li–Cu–Sn and Li–S products as specified by eq 1. After charging to 1.5 V, the Cu<sub>2</sub>SnS<sub>3</sub> peak reappears and becomes the most intensive in the fully charged sample (to 3 V), confirming the gradual reconversion of the Cu<sub>2</sub>SnS<sub>3</sub> phase as described in eq 2.

#### Discharge:



#### Charge:



The cycling performance of the CTS NPs, SNTs, and NTs is shown in Figure 7a. The capacity of the CTS NPs rapidly decreases in the first 30 cycles, resulting from the large volume expansion of the compact materials inside the large particles, and then gradually increases after pulverization with more exposed active materials, as confirmed by the *post-mortem* morphology of samples after 30 cycles (Figure S10). Because of the unstable structure of the CTS SNTs, the capacity drastically decays to below 500 mAh g<sup>-1</sup> after merely 15 cycles and then gradually fades upon further cycling. In contrast, after an activation process in the first 30 cycles, no further capacity degradation can be seen in the CTS NTs, and the charge capacity remains at 774 mAh g<sup>-1</sup>

even after 200 cycles. The Coulombic efficiency (CE) of the CTS NPs and NTs is close to 100% after the first several cycles, but the CE of the CTS SNTs is only up to ~95%, resulting from the SEI formation with substantial Li<sup>+</sup> consumption on the large surface area of the divided nanotubes.

The rate capability of the CTS NPs, SNTs, and NTs is compared in Figure 7b, and the theoretical specific current density is calculated in Supplementary Note 1. The CTS NTs exhibit the highest charge capacity at all rates, delivering ~600 mAh g<sup>-1</sup> at 1C, 67% and 31% more than that of the CTS NPs and SNTs, respectively. After returning to 0.2C, both the CTS NPs and SNTs deliver largely reduced capacity compared to the capacity in the first 10 cycles, while the CTS NTs deliver a comparable charge capacity of ~740 mAh g<sup>-1</sup>. The CTS NTs also deliver a favorable capacity of ~350 mAh g<sup>-1</sup> with 5C-rate tests after 200 cycles (Figure S11). The superior rate capability and cycling performance of the CTS NTs can be attributed to the hollow and porous nanotube structure, defined by the Cu<sub>3–4</sub>SnS<sub>4</sub> core and Cu<sub>2</sub>SnS<sub>3</sub> shell buffering volume expansion.

The initial charge/discharge profiles of the CTS NPs, SNTs, and NTs are shown in Figure 7c. The charge potential plateaus above 1.9 V are related to the regeneration of the CTS phase as presented in eq 2, which is usually unattainable and only observed in high capacity sulfide materials.<sup>24</sup> After the delithiation process, the CTS materials become more electrochemically reversible toward Li and thus exhibit a high and stable capacity. The charge capacity of the CTS NTs above 1.9 V (dashed line) is higher than that of the CTS NPs and SNTs, suggesting the more reversible CTS materials have been activated for lithiation.

Figure 7d–f display the charge/discharge curves of all the CTS nanomaterials. The initial CE of the CTS NPs, SNTs, and NTs is 80.3%, 58.9%, and 82.5%, elucidating the reduced side reactions and well-preserved active materials in the CTS NTs. The charge/discharge plateaus of the CTS NPs and SNTs fade apparently,

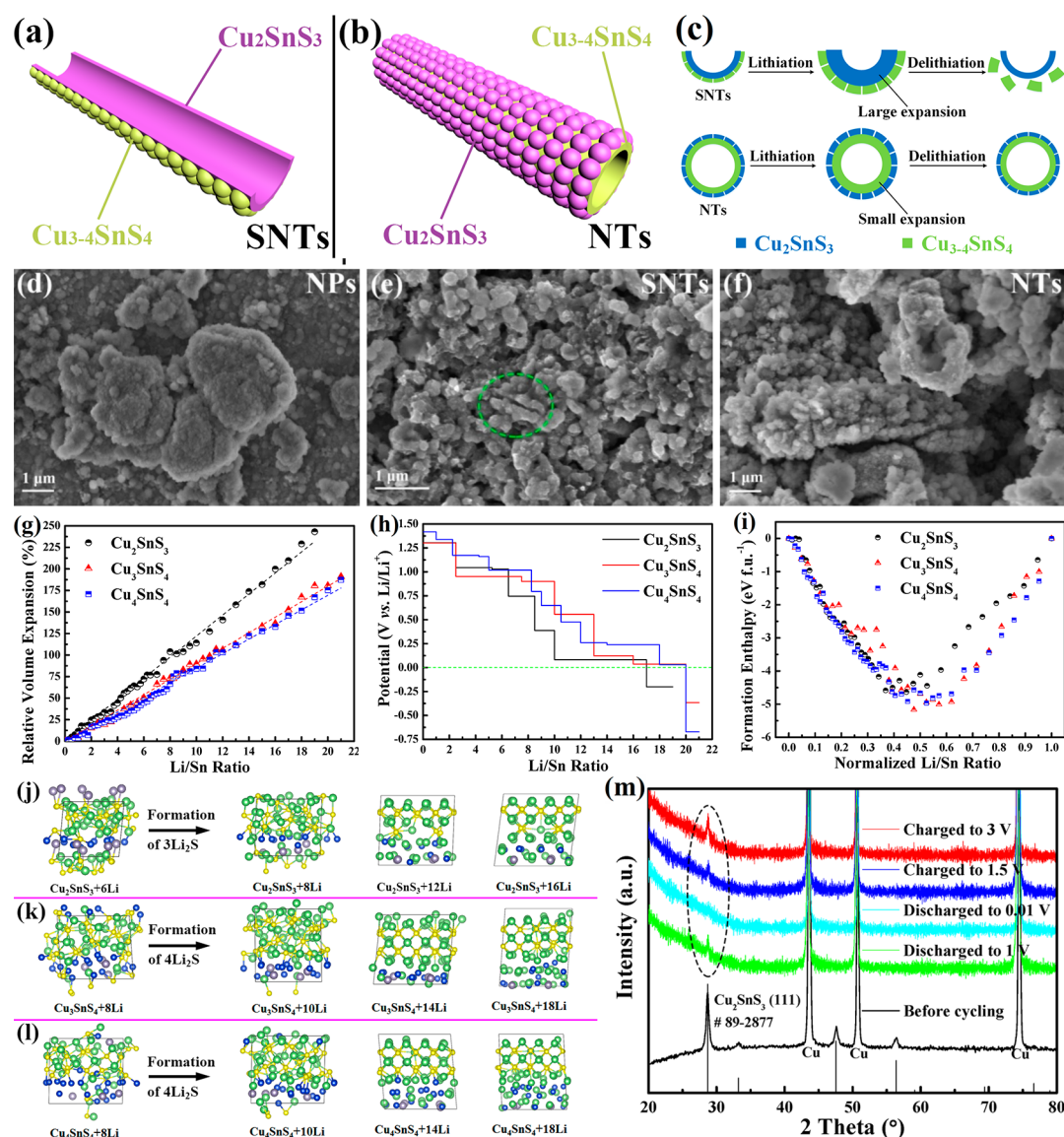


**Figure 6.** (a, b) Core-shell structures of CTS SNTs and NTs. (c) Schematic of volume expansion in CTS SNTs and NTs upon cycling. (d–f) *Post-mortem* morphology of CTS NPs, SNTs, and NTs after 200 cycles. (g) Relative volume expansion with linear regression lines and (h) calculated potentials as a function of Li/Sn ratio. (i) Formation enthalpy as a function of normalized Li/Sn ratio. Calculated atomic configurations for (j)  $\text{Cu}_2\text{SnS}_3$ , (k)  $\text{Cu}_3\text{SnS}_4$ , and (l)  $\text{Cu}_4\text{SnS}_4$ . Atomic coloring: Li, green; S, yellow; Cu, blue; Sn, gray. (m) *Ex situ* XRD patterns of CTS NPs initially discharged to 1/0.01 V and charged to 1.5/3 V.

while the ones of the CTS NTs remain stable, consistent with the DFT calculations suggesting that  $\text{Cu}_4\text{SnS}_4$  has a high potential profile and stability (Figure 6g–i). The capacity retention of the CTS NTs is also the highest among all the samples.

The cyclic voltammetry (CV) curves ( $0.1 \text{ mV s}^{-1}$ ) of the CTS NPs, SNTs, and NTs (Figure 8a–c) are consistent with the capacity differential plots (Figure S12). The peak labels are based on the reported CV curves of  $\text{CuS}^{25}$  and  $\text{SnS}_2$ .<sup>26</sup> In the range of 1–1.6 V, only two reduction peaks related to eq 1 can be found in the CTS NPs and SNTs (Figure 8a,b). In contrast, three reduction peaks exist in the CTS NTs (Figure 8c) related to the enhanced synergetic lithiation of Sn and Cu compounds. On one hand, the low formation enthalpy of  $\text{Cu}_4\text{SnS}_4$  (Figure 6i) is beneficial to the synergetic lithiation of Sn and Cu to form solid-solution phases.<sup>27</sup> On the other hand, the reduced volume expansion of alloying sulfides can facilitate the synthetic alloying reactions.<sup>28</sup> As a result, the CTS NTs with thermodynamic

stability and mitigated volume expansion exhibit the cooperative redox behaviors. Not only is the irreversible capacity of the CTS NTs the smallest, but also the difference between the oxidation and reduction potentials in each marked circle related to polarization is the smallest among all the samples.

After 200 cycles, the resistances of all samples are tested by electrochemical impedance spectroscopy (EIS) (Figure 8d). The origin intercept for the plot represents the internal resistance of the cell ( $R_s$ ), the semicircles in the middle- and low-frequency ranges represent the resistances of the SEI film ( $R_f$ ) and charge transfer interface ( $R_{ct}$ ), respectively, and the oblique line in the low-frequency range represents the Warburg impedance of  $\text{Li}^+$  diffusion ( $Z_w$ ). The constant phase elements are associated with the capacitances of the SEI film ( $\text{CPE}_1$ ) and charge transfer interface ( $\text{CPE}_2$ ), respectively. The equivalent circuit model and calculated parameters are shown in the inset of Figure 8d. Apparently, the SEI film and charge transfer resistances of the

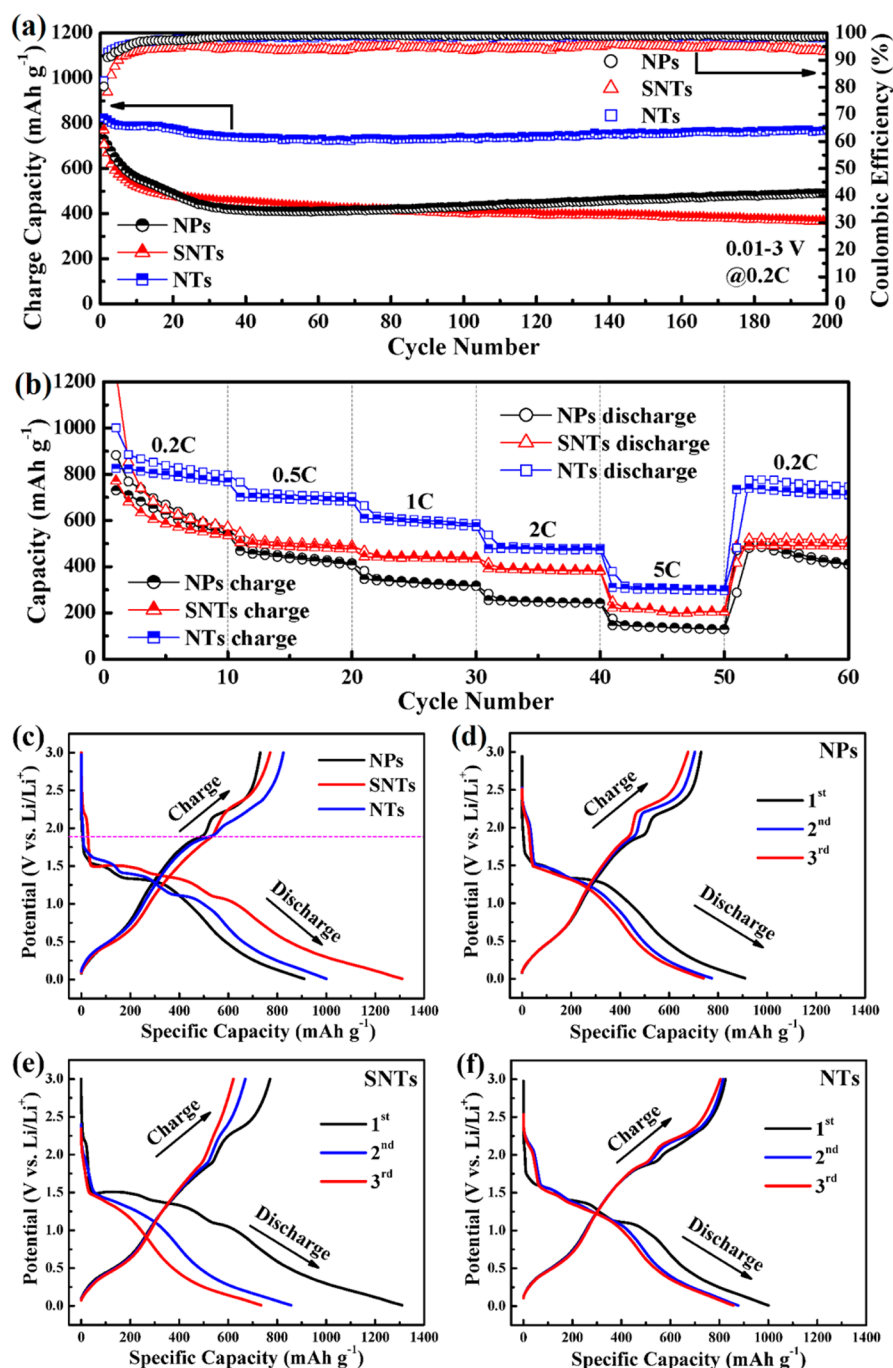


**Figure 7.** (a) Cycling performance and (b) rate capability of CTS NPs, SNTs, and NTs. Galvanostatic charge/discharge curves of (c) CTS NPs, SNTs, and NTs in the initial cycle and (d) CTS NPs, (e) CTS SNTs, and (f) CTS NTs in the first three cycles.

CTS NTs are both the smallest among all the samples, indicating the largely reduced electrochemical polarization by the stable nanostructure and the stable thermodynamics as informed by the DFT calculations (Figure 6g-i).

Compared with the previously reported results<sup>9–12</sup> for pure CTS materials for LIBs (Figure S13), the CTS NTs in this work exhibit superior cycling performance and rate capability, which can be fundamentally attributed to (i) the facile synthetic method with uniformly distributed materials and without heteroadditives; (ii) the porous and hollow nanotube structure for alleviating volume expansion; and (iii) the stable core-shell composition of  $\text{Cu}_{3-4}\text{SnS}_4@ \text{Cu}_2\text{SnS}_3$  and the abundant  $\text{Cu}_4\text{SnS}_4$  phase with superior properties for durable lithiation.

## CONCLUSIONS

Self-assembled Cu–Sn–S nanotubes, sub-nanotubes, and nanoparticles are fabricated by a facile gelation–solvothermal method, and the Cu–Sn–S nanotubes exhibit the best electrochemical properties with reduced polarization and enhanced reversible Cu–Sn–S materials. This phenomenon is ascribed to the mitigated volume expansion by the porous nanotube structure, the stable core–shell composition of  $\text{Cu}_{3-4}\text{SnS}_4@ \text{Cu}_2\text{SnS}_3$ , and the superior  $\text{Cu}_4\text{SnS}_4$  phase as calculated with DFT. The structural changes of different Cu–Sn–S stoichiometries demonstrate that Cu is advantageous for generating Li–Cu–S compounds with a high potential and lithiation capacity. This work provides

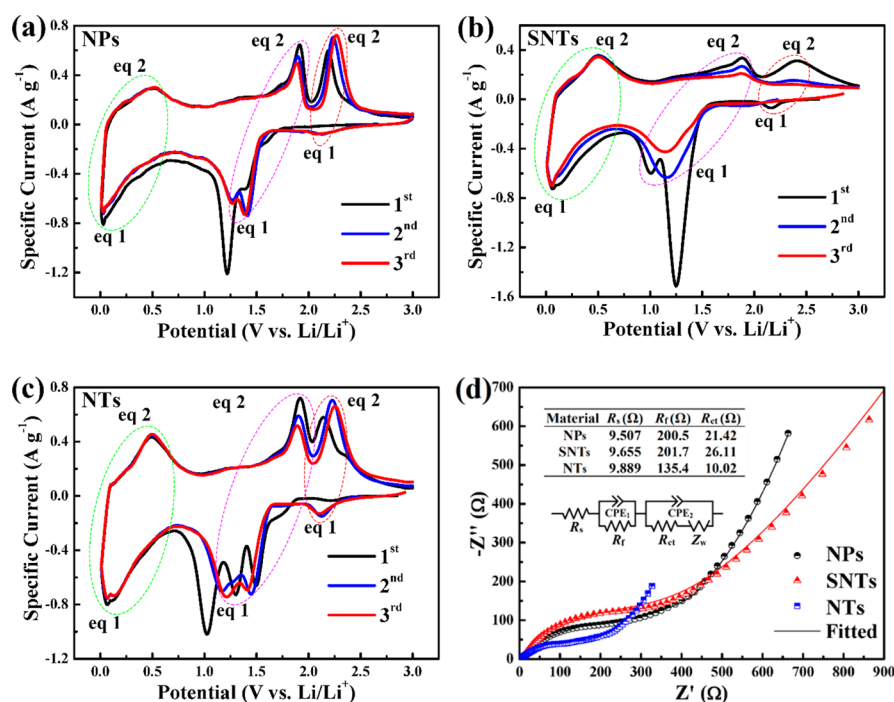


Figure 8. (a–c) CV curves of CTS NPs, SNTs, and NTs in the first three cycles. (d) EIS plots with fitted lines of CTS NPs, SNTs, and NTs after 200 cycles. Inset is calculated parameters and fitting equivalent circuit model.

guidance for systematically developing new nanotube materials and theoretically studying advanced ternary electrodes for energy storage.

## METHODS

**Synthesis of CTS NPs, SNTs, and NTs.** As illustrated in Scheme 1, the CTS NTs and SNTs were synthesized *via* gelation followed by a solvothermal method using CuCl and CuCl<sub>2</sub>·2H<sub>2</sub>O as the Cu sources, respectively. The CTS NPs were prepared *via* dipping followed by a solvothermal method using CuCl as the Cu source. In the first step, Tu (4 mmol) was dissolved by vigorous stirring in 20 mL of ethanol to form a transparent solution. Meanwhile, CuCl (for CTS NTs) or CuCl<sub>2</sub>·2H<sub>2</sub>O (for CTS SNTs) (2 mmol) was mixed with SnCl<sub>4</sub>·5H<sub>2</sub>O (1 mmol) by vigorous stirring in 20 mL of ethanol to form a uniform solution. In the second step, the above Tu and chloride solutions were mixed promptly, producing a [Cu(Tu)<sub>2</sub>]Cl complex and converting into a white gel after vigorous stirring as described in eqs S1 and S2. In the third step, the CTS NTs/SNTs gels and the CTS NPs solution were transferred to three Teflon-lined stainless steel autoclaves and kept at 160 °C for 15 h. After naturally cooling to ambient temperature, the black precipitates in the autoclaves were centrifuged, washed with deionized water and ethanol several times, and vacuum-dried at 60 °C for 12 h. In the last step, the final products were annealed in a tube furnace at 400 °C for 4 h under Ar gas flow with a heating rate of 3 °C min<sup>-1</sup>. The four steps resulted in producing composites of Cu<sub>2</sub>SnS<sub>3</sub>, Cu<sub>3</sub>SnS<sub>4</sub>, and Cu<sub>4</sub>SnS<sub>4</sub> with different ratios and nanostructures as specified in eqs S3, S4, and S5.

**Characterization.** A Quanta FEG 650 SEM was used for imaging and detecting EDS. A JEOL 2010F TEM was used for checking nano-scale morphology, crystal structure, and elemental distribution. XRD patterns were obtained by using a Rigaku MiniFlex 600 diffractometer. Rietveld refinement analysis was performed using the HighScore Plus software based on the atomic structures of Cu<sub>2</sub>SnS<sub>3</sub> [JCPDS 89-2877], Cu<sub>3</sub>SnS<sub>4</sub> [JCPDS 36-0217], and Cu<sub>4</sub>SnS<sub>4</sub> [JCPDS 71-0129], with a subsequent relaxation using DFT. XPS and Auger spectra were obtained by using a Kratos Axis Ultra DLD instrument. Surface areas and porosity were obtained from N<sub>2</sub>-sorption isotherms measured at 77 K (Quantachrome, Nova 2200e).

**Electrochemical Measurements.** The CTS NPs, SNTs, and NTs were dispersed in deionized water with 90 kDa carboxymethyl cellulose (CMC) binder and Super P Li carbon to form an 8:1:1 weight ratio slurry. The slurry was coated on Cu foils using a notch bar and dried at 120 °C for 12 h in a vacuum oven. The mass loading of each electrode was 0.3–0.5 mg cm<sup>-2</sup>. Coin cells (CR2032) were assembled in an argon-filled glovebox with lithium foil anodes, polypropylene membranes (Celgard 2400) separators, and 1.0 M LiPF<sub>6</sub> in ethylene carbonate/diethyl carbonate (1:1 v/v) electrolyte. The galvanostatic charge/discharge tests were conducted on a battery tester (Arbin, BT 2143) between 0.01 and 3 V. EIS plots were obtained using a potentiostat (CHI 608D) with an amplitude potential of 5 mV from 10<sup>6</sup> to 10<sup>-1</sup> Hz.

**Calculation Details.** To calculate the electronic structure, volume expansion, lithiation potentials formation enthalpy, and structural changes upon lithiation of the CTS materials, spin-polarized DFT with a generalized gradient approximation parametrized by Perdew–Burke–Ernzerhof<sup>29</sup> as implemented in the Vienna *ab initio* simulation package were applied.<sup>30</sup> Core electrons were described within the projector-augmented wave framework, and valence electrons were expanded in a plane-wave basis set. The kinetic energy cutoff of the plane-wave basis was set to 500 eV for structural relaxation and 300 eV for basin-hopping optimization. The *k*-point meshes for the integration of the Brillouin zone were determined by convergence tests achieving a total energy per formula unit (f.u.) within 2.0 meV. For all calculations, both ionic positions and cell parameters were fully relaxed. To describe the strong correlation between 3d-orbital electrons of the transition metals, a Hubbard *U* correction was adopted, where a *U*<sub>eff</sub> value of 9.0 eV for Cu was chosen based upon previous work.<sup>31</sup> Four f.u.'s of Cu<sub>2</sub>SnS<sub>3</sub>/Cu<sub>4</sub>SnS<sub>4</sub> and two f.u.'s of Cu<sub>3</sub>SnS<sub>4</sub> were used for structural relaxation of interstitial lithiation. Four f.u.'s of Cu<sub>2</sub>SnS<sub>3</sub>, Cu<sub>3</sub>SnS<sub>4</sub>, and Cu<sub>4</sub>SnS<sub>4</sub> were used for global optimization calculations with the basin-hopping algorithm.<sup>32</sup>

## ASSOCIATED CONTENT

### Supporting Information

The Supporting Information is available free of charge on the ACS Publications website at DOI: 10.1021/acsnano.7b05294.

Comparison with Cu/Sn-based sulfides, reaction mechanisms, surface areas and porosity, XRD refinements,

STEM elemental analysis, cross-section SEM images of nanotubes, XPS peaks, deformation analysis, *ex situ* XRD patterns, *post-mortem* SEM images, long-term 5C test, capacity differential plots, comparison with reported CTS materials, and theoretical capacity calculations (PDF)

## AUTHOR INFORMATION

### Corresponding Authors

\*E-mail (H. Guo): [hangguo@xmu.edu.cn](mailto:hangguo@xmu.edu.cn).

\*E-mail (G. Henkelman): [henkelman@utexas.edu](mailto:henkelman@utexas.edu).

\*E-mail (C.B. Mullins): [mullins@che.utexas.edu](mailto:mullins@che.utexas.edu).

### ORCID

Jie Lin: 0000-0002-1281-9713

Kenta Kawashima: 0000-0001-7318-6115

Yang Liu: 0000-0002-7240-1546

Hang Guo: 0000-0001-9062-9678

Graeme Henkelman: 0000-0002-0336-7153

Charles Buddie Mullins: 0000-0003-1030-4801

### Notes

The authors declare no competing financial interest.

## ACKNOWLEDGMENTS

This work was supported by the Welch Foundation through grants F-1131 (A.H.), F-1841 (G.H.), and F-1436 (C.B.M.) as well as the National Science Foundation through grant number CBET-1603491 (C.B.M.). J. Lin thanks Karalee Jarvis, Dwight Romanovic, Shouliang Zhang, Hugo Celio, Jiarui He, Edward Evans, and Gearba Raluca for the characterization assistance. We also acknowledge the China Scholarship Council (CSC) scholarship under the State Scholarship Fund.

## REFERENCES

- (1) Youn, D. H.; Stauffer, S. K.; Xiao, P.; Park, H.; Nam, Y.; Dolocan, A.; Henkelman, G.; Heller, A.; Mullins, C. B. Simple Synthesis of Nanocrystalline Tin Sulfide/N-Doped Reduced Graphene Oxide Composites as Lithium Ion Battery Anodes. *ACS Nano* **2016**, *10*, 10778–10788.
- (2) Seo, J.-w.; Jang, J.-t.; Park, S.-w.; Kim, C.; Park, B.; Cheon, J. Two-Dimensional SnS<sub>2</sub> Nanoplates with Extraordinary High Discharge Capacity for Lithium Ion Batteries. *Adv. Mater.* **2008**, *20*, 4269–4273.
- (3) Qu, B.; Ma, C.; Ji, G.; Xu, C.; Xu, J.; Meng, Y. S.; Wang, T.; Lee, J. Y. Layered SnS<sub>2</sub>-Reduced Graphene Oxide Composite—a High-Capacity, High-Rate, and Long-Cycle Life Sodium-Ion Battery Anode Material. *Adv. Mater.* **2014**, *26*, 3854–9.
- (4) Zhou, T.; Pang, W. K.; Zhang, C.; Yang, J.; Chen, Z.; Liu, H. K.; Guo, Z. Enhanced Sodium-Ion Battery Performance by Structural Phase Transition from Two-Dimensional Hexagonal-SnS<sub>2</sub> to Orthorhombic-SnS. *ACS Nano* **2014**, *8*, 8323–33.
- (5) Winter, M.; Besenhard, J. O. Electrochemical Lithiation of Tin and Tin-Based Intermetallics and Composites. *Electrochim. Acta* **1999**, *45*, 31–50.
- (6) Wu, F.; Yushin, G. Conversion Cathodes for Rechargeable Lithium and Lithium-Ion Batteries. *Energy Environ. Sci.* **2017**, *10*, 435–459.
- (7) Coughlan, C.; Ibanez, M.; Dobrozhan, O.; Singh, A.; Cabot, A.; Ryan, K. M. Compound Copper Chalcogenide Nanocrystals. *Chem. Rev.* **2017**, *117*, 5865–6109.
- (8) Wu, C.; Hu, Z.; Wang, C.; Sheng, H.; Yang, J.; Xie, Y. Hexagonal Cu<sub>2</sub>SnS<sub>3</sub> with Metallic Character: Another Category of Conducting Sulfides. *Appl. Phys. Lett.* **2007**, *91*, 143104.
- (9) Qu, B.; Li, H.; Zhang, M.; Mei, L.; Chen, L.; Wang, Y.; Li, Q.; Wang, T. Ternary Cu<sub>2</sub>SnS<sub>3</sub> Cabbage-Like Nanostructures: Large-Scale Synthesis and Their Application in Li-Ion Batteries with Superior Reversible Capacity. *Nanoscale* **2011**, *3*, 4389–93.

(10) Qu, B.; Zhang, M.; Lei, D.; Zeng, Y.; Chen, Y.; Chen, L.; Li, Q.; Wang, Y.; Wang, T. Facile Solvothermal Synthesis of Mesoporous Cu<sub>2</sub>SnS<sub>3</sub> Spheres and Their Application in Lithium-Ion Batteries. *Nanoscale* **2011**, *3*, 3646–3651.

(11) Nie, L.; Zhang, Y.; Ye, K.; Han, J.; Wang, Y.; Rakesh, G.; Li, Y.; Xu, R.; Yan, Q.; Zhang, Q. A Crystalline Cu–Sn–S Framework for High-Performance Lithium Storage. *J. Mater. Chem. A* **2015**, *3*, 19410–19416.

(12) Zhang, Z.; Fu, Y.; Zhou, C.; Li, J.; Lai, Y. EDTA-Na<sub>2</sub>-Assisted Hydrothermal Synthesis of Cu<sub>2</sub>SnS<sub>3</sub> Hollow Microspheres and Their Lithium Ion Storage Performances. *Solid State Ionics* **2015**, *269*, 62–66.

(13) Zhang, Z.; Zhou, C.; Jia, M.; Fu, Y.; Li, J.; Lai, Y. Synthesis of Copper Tin Sulfide/Reduced Graphene Oxide Composites and Their Electrochemical Properties for Lithium Ion Batteries. *Electrochim. Acta* **2014**, *143*, 305–311.

(14) Tao, H.-C.; Zhu, S.-C.; Yang, X.-L.; Zhang, L.-L.; Ni, S.-B. Reduced Graphene Oxide Decorated Ternary Cu<sub>2</sub>SnS<sub>3</sub> as Anode Materials for Lithium Ion Batteries. *J. Electroanal. Chem.* **2016**, *760*, 127–134.

(15) Rui, X.; Tan, H.; Yan, Q. Nanostructured Metal Sulfides for Energy Storage. *Nanoscale* **2014**, *6*, 9889–924.

(16) Wu, X.; Zhang, S.; Fang, H.; Du, Z.; Lin, R. Feasibility of Utilizing Three-Dimensional Nanoarchitecture to Endow Metal Sulfides with Superior Li<sup>+</sup> Storage Capability. *J. Power Sources* **2014**, *264*, 311–319.

(17) Wu, P.; Du, N.; Zhang, H.; Liu, J.; Chang, L.; Wang, L.; Yang, D.; Jiang, J. Z. Layer-Stacked Tin Disulfide Nanorods in Silica Nanoreactors with Improved Lithium Storage Capabilities. *Nanoscale* **2012**, *4*, 4002–6.

(18) Zou, Y.; Wang, Y. Sn@CNT Nanostructures Rooted in Graphene with High and Fast Li-Storage Capacities. *ACS Nano* **2011**, *5*, 8108–14.

(19) Li, S.; Zuo, S.; Wu, Z.; Liu, Y.; Zhuo, R.; Feng, J.; Yan, D.; Wang, J.; Yan, P. Stannous Sulfide/Multi-Walled Carbon Nanotube Hybrids as High-Performance Anode Materials of Lithium-Ion Batteries. *Electrochim. Acta* **2014**, *136*, 355–362.

(20) Yella, A.; Mugnaioli, E.; Panthofer, M.; Thereise, H. A.; Kolb, U.; Tremel, W. Bismuth-Catalyzed Growth of SnS<sub>2</sub> Nanotubes and Their Stability. *Angew. Chem., Int. Ed.* **2009**, *48*, 6426–30.

(21) Sun, Y. K.; Myung, S. T.; Park, B. C.; Prakash, J.; Belharouak, I.; Amine, K. High-Energy Cathode Material for Long-Life and Safe Lithium Batteries. *Nat. Mater.* **2009**, *8*, 320–4.

(22) Sun, Y. K.; Chen, Z.; Noh, H. J.; Lee, D. J.; Jung, H. G.; Ren, Y.; Wang, S.; Yoon, C. S.; Myung, S. T.; Amine, K. Nanostructured High-Energy Cathode Materials for Advanced Lithium Batteries. *Nat. Mater.* **2012**, *11*, 942–7.

(23) Lin, F.; Nordlund, D.; Li, Y.; Quan, M. K.; Cheng, L.; Weng, T.-C.; Liu, Y.; Xin, H. L.; Doeff, M. M. Metal Segregation in Hierarchically Structured Cathode Materials for High-Energy Lithium Batteries. *Nature Energy* **2016**, *1*, 15004.

(24) Lin, J.; Guo, J.; Liu, C.; Guo, H. Ultrahigh-Performance Cu<sub>2</sub>ZnSnS<sub>4</sub> Thin Film and Its Application in Microscale Thin-Film Lithium-Ion Battery: Comparison with SnO<sub>2</sub>. *ACS Appl. Mater. Interfaces* **2016**, *8*, 34372–34378.

(25) Du, Y.; Yin, Z.; Zhu, J.; Huang, X.; Wu, X. J.; Zeng, Z.; Yan, Q.; Zhang, H. A General Method for the Large-Scale Synthesis of Uniform Ultrathin Metal Sulphide Nanocrystals. *Nat. Commun.* **2012**, *3*, 1177–1183.

(26) Kim, T.-J.; Kim, C.; Son, D.; Choi, M.; Park, B. Novel SnS<sub>2</sub>-Nanosheet Anodes for Lithium-Ion Batteries. *J. Power Sources* **2007**, *167*, 529–535.

(27) Wang, F.; Kim, S. W.; Seo, D. H.; Kang, K.; Wang, L.; Su, D.; Vajo, J. J.; Wang, J.; Graetz, J. Ternary Metal Fluorides as High-Energy Cathodes with Low Cycling Hysteresis. *Nat. Commun.* **2015**, *6*, 6668.

(28) Lin, J.; Guo, J.; Liu, C.; Guo, H. Three-Dimensional Cu<sub>2</sub>ZnSnS<sub>4</sub> Films with Modified Surface for Thin-Film Lithium-Ion Batteries. *ACS Appl. Mater. Interfaces* **2015**, *7*, 17311–17317.

(29) Perdew, J. P.; Burke, K.; Ernzerhof, M. Generalized Gradient Approximation Made Simple. *Phys. Rev. Lett.* **1996**, *77*, 3865–3868.

(30) Kresse, G.; Furthmüller, J. Efficiency of *Ab-Initio* Total Energy Calculations for Metals and Semiconductors Using a Plane-Wave Basis Set. *Comput. Mater. Sci.* **1996**, *6*, 15–50.

(31) Lim, J.-M.; Hwang, T.; Park, M.-S.; Cho, M.; Cho, K. Design of a P-Type Electrode for Enhancing Electronic Conduction in High-Mn, Li-Rich Oxides. *Chem. Mater.* **2016**, *28*, 8201–8209.

(32) Wales, D. J.; Doye, J. P. K. Global Optimization by Basin-Hopping and the Lowest Energy Structures of Lennard-Jones Clusters Containing up to 110 Atoms. *J. Phys. Chem. A* **1997**, *101*, 5111–5116.